Engineering xxx (xxxx) xxx

Contents lists available at ScienceDirect

Engineering

journal homepage: www.elsevier.com/locate/eng

Civil Engineering Material—Article

Breakthrough of Carbon–Ash Recalcitrance in Hydrochar via Molten Carbonate: Engineering Mineral-Rich Biowaste towards Sustainable Platform Carbon Materials

Zihan Wang [a], Leli Zhang [a], Yuanhui Zhang [b], Zhidan Liu [a,*]

[a] Laboratory of Environment-Enhancing Energy (E2E), Key Laboratory of Agricultural Engineering in Structure and Environment, Ministry of Agriculture, College of Water Resources and Civil Engineering, China Agricultural University, Beijing 100083, China
[b] Department of Agricultural and Biological Engineering, University of Illinois at Urbana-Champaign, Urbana, IL 61801, USA

ARTICLE INFO

Article history:
Available online xxxx

Keywords:
Hydrochar
Livestock manure
Ammonia adsorption
Deashing
Oxygen activation

ABSTRACT

The function-led design of porous hydrochar from mineral-rich biowaste for environmental applications inevitably suffers from carbon–ash recalcitrance. However, a method to alter the original carbon skeleton with ash remains elusive and hinders the availability of hydrochar. Herein, we propose a facile strategy for breaking the rigid structure of carbon–ash coupled hydrochar using phase-tunable molten carbonates. A case system was designed in which livestock manure and sodium bicarbonate ($NaHCO_3$) were used to prepare the activated hydrochar, and ammonia (NH_3) served as the target contaminant. Due to the redox effect, we found that organic fractions significantly advanced the melting temperature of sodium carbonate (Na_2CO_3) below 800 °C. The sodium (Na) species steadily broke the carbon–ash interaction as the thermal intensity increased and transformed inorganic constituents to facilitate ash dissolution, rebuilding the hydrochar skeleton with abundant hierarchical channels and active defect edges. The surface polarity and mesopore distribution collectively governed the five-cycle NH_3 adsorption attenuation process. Manure hydrochar delivered favorable potential for application with a maximum overall adsorption capacity of 100.49 $mg \cdot g^{-1}$. Integrated spectroscopic characterization and theoretical computations revealed that incorporating NH_3 on the carbon surface could transfer electrons to chemisorbed oxygen, which promoted the oxidation of pyridine-N during adsorption. This work offers deep insight into the structure-function correlation of hydrochar and inspires a more rational design of engineered hydrochar from high-ash biowaste.

1. Introduction

Driven by the ever-growing global population, rapid industrial development, and urbanization, the demand for natural resources continues to increase, causing tremendous waste production and severe threats to planetary stability and human well-being [1]. Innovating valorization strategies for biowaste streams to promote reduction, reuse, and recycling at distinct levels is closely connected to targeting the United Nations' Sustainable Development Goals [2,3]. Developing biochar materials to convert renewable resources is ideal for addressing many global issues [4]. Biochar, a carbon-rich material converted from biomass by pyrolysis, gasification, torrefaction, and hydrothermal carbonization (HTC), has stimulated significant interest in climate regulation and food security over the past few decades [5–7]. Biochar is an emerging tool for carbon sequestration owing to its economical and sustainable properties and high environmental application potential as a functional material, including contaminant immobilization, nutrient recovery, and energy storage [8–11].

Notably, rich biomass waste resources endow biochar with diverse properties and compositions, especially in terms of structural and inorganic components, contributing to the enormous uncertainty and heterogeneity of hydrochar structures [12]. Exogenous and inherent minerals can be immobilized by embedding and chelating reactions with a carbon matrix, leading to numerous obstacles in practical applications [13,14]. In fact, carbon–ash coupling frameworks exist widely in carbon materials prepared from biomass with high ash content (e.g., livestock manure, sewage

* Corresponding author.
E-mail address: zdliu@cau.edu.cn (Z. Liu).

https://doi.org/10.1016/j.eng.2024.01.009

Please cite this article as: Z. Wang, L. Zhang, Y. Zhang et al., Breakthrough of Carbon–Ash Recalcitrance in Hydrochar via Molten Carbonate: Engineering Mineral-Rich Biowaste towards Sustainable Platform Carbon Materials, Engineering, https://doi.org/10.1016/j.eng.2024.01.009

sludge, rice straw) [15–18]. To further enhance the application performance, the design and modulation of biochar are inevitably required by introducing chemical activators and innovative activation methods to rebuild skeletal structures [19–21]. Elucidating the carbon–ash interaction of biochar is vital for establishing structure-application relationships.

Residual ash, typically included in the organic matrix mixture and structural constituents, is collectively responsible for the recalcitrance of biochars fabricated using distinct technologies [12,22]. Some mechanisms have been proposed to explain this effect: ① The intertwined ash and active components can reduce the carbonaceous structure accessibility by encapsulating the carbon matrix [23]; ② minerals serve as barriers to block the diffusion of heat and constrict the release of volatiles during the charring process [24]; and ③ condensed aromatic C confers distinct oxidation resistance and thermal stability to biochar [25]. Mutual protection between the inorganic and organic phases plays an important role in the biogeochemical cycling of biochar [26]. It has been reported that the gradually intense carbon cracking reaction caused the fracture of organic layers and the exposure of silicon layers to increasing pyrolytic temperatures, significantly improving the silicon dissolution performance of biochar [27]. This demonstrated that the rigidity of the carbon structure was crucial for the ash release. Hydrothermal conversion arms produce hydrochar with a high carbon content, well-developed aromatic nature, and abundant insoluble minerals, as determined by feedstock, compared with pyrochar prepared from pyrolysis [28]. In addition, owing to the differences in the carbonization mechanism, minerals can be effectively protected and dispersed during the aromatization and nuclear reaction of organic matter in HTC [29]. This indicates that hydrochar offers greater chemical recalcitrance and resistance to decomposition during post-carbonization [7]. For predicting the fate and reactivity of hydrochar, it appears crucial to link the evolution of the carbon–ash structure of char to its physicochemical properties.

Generally, supplementation with additional salts to construct a multi-component mixture system can alter the thermal and chemical stabilities of mineral constituents in chars and produce porous carbons with excellent porosity and distinct microstructures [30–32]. Molten salts facilitate the cleavage of metal ions or ionic/covalent bonds by providing intermediate active substances in a strong polarization environment [33,34], whereas the catalytic performance is determined by the properties of the molten salts and carbon precursors, such as melting temperature, thermal stability, and chemical components [35]. Molten carbonate salts are considered optimal media for the chemical cracking reactions of molecular organic functional groups (OFGs) and structures. They are also effective in dissolving metal compounds, such as silicon dioxide, but are limited by their high melting points [36,37]. Several studies have investigated the interactions of O-containing functional groups on carbon surfaces with salts [33,38]. To date, the transformation and morphology of carbonate salts during the activation and breakthrough of the recalcitrance of hydrochar, especially that derived from high-ash biomass, remain unclear.

In response to the above knowledge gaps, we endeavor: ① to clarify the breaking mechanism of high-ash hydrochar recalcitrance during molten salts activation, involving the interaction C-ash system of manure hydrochar with sodium carbonate, along with the effect of chemical components of hydrochar on the transformation of sodium carbonate, by X-ray photoelectron spectroscopy (XPS), differential scanning calorimeter (DSC), and scanning electron microscope (SEM) analyses and so forth; ② to introduce ammonia (NH_3) as the target contaminant to investigate the relationship of hierarchical structure of hydrochar with NH_3 and determine the role of surface functionality in NH_3 immobilization through fix-bed NH_3 adsorption test and density functional theory (DFT).

2. Materials and methods

2.1. Feedstock and chemical reagents

Cow manure (CM) and pig manure (PM), which are typical high-ash livestock wastes, were collected from local farms in Pinggu District, Beijing, China. The fresh manures were stored at −20 °C and sealed with plastic bags before further usage. The detailed composition of the feedstock is provided in Table S1 in Appendix A.

For the HTC process, the thawed manure was first dried at (80 ± 5) °C in the oven and was ground and passed through a 1.70 mm sieve. The slurry, which was mixed with the manure powder and deionized water (DI) with a total solid content of 20%, was transferred into a stainless-steel hydrothermal reactor (500 mL) (Parr 4848; Parr Instrument Co., USA) for hydrochar preparation. The sealed reactor was heated electrically to varied temperatures, ranging from 190 to 260 °C at intervals of 20 °C, and then maintained for 2 h under autogenous pressure. The solid residue was collected by vacuum filtration and then immersed in 1 L of hydrogen chloride (HCl) solution (0.1 $mol \cdot L^{-1}$) to remove the inorganic components. DI water was continuously used to wash the acid residue on the carbon surface until the pH of the supernatant was nearly neutral. The carbon samples were dried overnight at 105 °C in the oven afterward. The obtained CM and PM hydrochars, wherein samples produced at 230 °C were employed as precursors for activation and referred to as HC and HP, respectively, were smashed and stored for subsequent characterization.

Sodium bicarbonate ($NaHCO_3$, ≥ 85%, Macklin Inc., China) was the activator for breaking the carbon–ash interaction. After thoroughly grinding HC and HP with $NaHCO_3$ (hydrochar/activator ratio of 1:2), the mixtures (9.0 g) were weighed into a tube furnace and pyrolyzed at specific temperatures (500, 650, and 800 °C) with a heating rate of 10 $°C \cdot min^{-1}$ and 2 h duration under nitrogen (N_2) flow (350 $mL \cdot min^{-1}$). The activator was absent during the conventional pyrolysis of HC and HP. Similarly, the resulting solid chars were subjected to the aforementioned washing process, wherein for $NaHCO_3$-activated hydrochar, the pickling was terminated when no more bubbles were produced in the suspension. After being dried and separated, the processed activated hydrochars derived from CM and PM were labeled as AHC-*X* and AHP-*X*, respectively, where *X* (*X* = 500, 650, and 800 °C) represented the pyrolysis temperatures. The thermal-treated hydrochars without introducing an activator were similarly denoted as "HC-*X*" and "HP-*X*", respectively.

2.2. Characterization

The thermogravimetry-infrared spectroscopy (TG-IR; STA 449F5 INVENIO-R, Bruker, Germany) experiments were performed to analyze the gaseous products volatilized during pyrolysis process with the temperature elevating from 30 to 1000 °C at a ramp rate of 10 $°C \cdot min^{-1}$ in N_2 stream. The melting point, enthalpy, and thermodynamic processes were determined using a TG-DSC (1100LF, Mettler Toledo, Switzerland). XPS (ESCALAB 250Xi, Thermo Fisher Scientific, USA) was used to analyze the elemental composition and valence states of the hydrochars. The distribution of elements (C, H, and N) was determined using a CHNS/O analyzer (Vario EL III, Elementar, Germany). The ash of feedstocks and hydrochars produced at 600 °C in a muffle oven under an air atmosphere for 4 h was analyzed by X-ray fluorescence (XRF; Supermini200, Rigaku, Japan). The mineral phases of samples were

characterized by an X-ray diffractometer (XRD; Rigaku Ultima IV, Rigaku) with Cu Kα radiation at a scanning rate of 5 (°)·min^{-1}. Surface morphology and elemental mapping details were observed using SEM (SU3500, Hitachi, Japan) coupled with energy-dispersive spectrometry (EDS; SU3500, Hitachi, Japan) and high-resolution transmission electron microscopy (TEM; Talos F200S, Thermo Fisher Scientific). Based on the Brunauer–Emmett–Teller (BET) method, the surface areas and pore volumes were determined by N_2 adsorption at 77 K (ASAP 2460, Micromeritics, USA). The aromatic ring structures of the materials were studied using Raman spectroscopy (LabRAM HR Evolution, Horiba Scientific, Japan).

2.3. Dynamic adsorption experiments of NH_3

The NH_3 adsorption performances of the hydrochars were evaluated using a laboratory-type fixed-bed adsorption instrument. The breakthrough curves and adsorption capacities were analyzed under distinct parameters, including temperatures (25, 40, and 70 °C), surface humidity (0 and 20 wt%), and five cycle adsorption–desorption test. Details are provided in Supplementary Text S1 in Appendix A. AHC-*X*-E and AHP-*X*-E represented the activated hydrochar derived from CM and PM after adsorption saturation, and the sample after desorption was labeled by AHC-*X*-D and AHP-*X*-D.

2.4. Computational method

The interaction energies of the carbon structure with the NH_3 molecule were calculated using DFT and performed using Gaussian 16 software (Revision A.03; Gaussian Inc., USA) and Multiwfn [39,40]. The energy barrier between the initial and final states was calculated to analyze the potential oxidation reaction of the N-containing groups triggered by active oxygen species during NH_3 exposure. The detailed implementations are described in Supplementary Text S2 in Appendix A.

3. Results and discussion

3.1. The interaction of carbon surface and $NaHCO_3$

The thermal properties of the hydrochar and $NaHCO_3$ mixtures were analyzed to reveal the activation mechanism involving thermal stability and gaseous product distribution. A more obvious adsorption band, assigned to the carbon dioxide (CO_2) at 2450–2250 cm^{-1} during the temperature 700–800 °C, was observed according to TG-IR spectra (Fig. S1 in Appendix A) after the introduction of $NaHCO_3$, indicating an intense mutual reaction between the carbonate and organic components of the hydrochars. For $NaHCO_3$, the thermogravimetric analysis curves (Fig. S2 in Appendix A) shifted towards lower temperatures in the presence of hydrochar, which was likely due to the effect of the surface chemical properties of hydrochar on the volatilization activation energy [41]. DSC analysis (Fig. 1(a)) shows the heat changes of $NaHCO_3$ and their correlation with the ash of manure hydrochar and cellulose- ($H_{cellulose}$), lignin- (H_{lignin}), and protein- ($H_{protein}$) based hydrochar. Notably, the decomposition of $NaHCO_3$ was significantly boosted by the above monocomponent hydrochars, with the decline of the melting points from 845.65 to 771.41 °C. At the same time, the introduction of ash, which altered the thermal properties of molten salts by forming new eutectic systems, exhibited slight impacts [32]. These changes demonstrate the occurrence of oxidation/reduction chemical reactions during activation, primarily induced by the OFGs of the hydrochar, which accelerate the transformation of sodium (Na) species to the corresponding atomic forms. The rich, accessible OFGs served as active sites for cation-anion interactions, which could alter the $NaHCO_3$ atomization mechanisms, leading to the advanced evaporation of oxides and Na.

The graphitization and defect degrees of the activated hydrochars were analyzed using Raman spectroscopy (Fig. S3 in Appendix A), wherein the characteristic peaks at 1350 and 1580 cm^{-1} corresponded to the disordered graphite structure (D-band) and the graphitized structure which is assigned to the stretching of carbon atoms pairs of sp^2 domains (G-band), respectively [42]. The relative intensity of the D-band/ G-band peak is commonly employed to estimate the type and density of defects, as well as the level of functionalization in a carbon material, owing to the inevitable disruption of symmetry by local structural and chemical defects [43]. The intensity ratios of the G peaks to D peaks (I_G/I_D) of CM and PM hydrochars gradually decreased from 1.25 and 1.14 to 0.99 and 0.98 as activation temperature escalated, respectively. This result suggesting more defect sites were generated thanks to the attack of aromatic ring matrix by molten salts, which facilitated the exposure of active sites on the edge of the carbon layer and the activation of chemisorbed oxygen species to O_2^- [44–46].

XPS was used to confirm the carbon configuration estimation further (Fig. S4 in Appendix A, Fig. 1(b)). The C 1s spectra could be deconvoluted to four peaks, including C=C ((284.6 ± 0.2) eV), C–O ((285.9 ± 0.2) eV), C=O ((287.3 ± 0.3) eV) and O=C–OR ((288.8 ± 0.4) eV) [47,48]. In contrast to the pyrolysis process without $NaHCO_3$ addition, the peaks of C=C decreased with increasing activation intensity, which agreed with the results of the abovementioned Raman analysis. In the O 1s peaks, the binding energy of (530.8 ± 0.4) eV, (532.8 ± 0.2) eV, and (534.1 ± 0.1) eV corresponded to C=O in carbonyl or quinine (O-I), C–O bond in phenol or ethers (O-II) and C–O in lactone or carboxylic anhydride (O-III), respectively [49,50]. The scarce content of O-I in hydrochars activated at 800 °C temperature demonstrated the decomposition of functional groups related to aromatization. The addition of $NaHCO_3$ accelerated the cracking of C=O groups, which released large amounts of free radicals, while Na species such as Na_2O integrated with vacancies at the edge of the carbon matrix, leading to an increase in C–O groups [33]. These exothermic chemical reactions during carbonization and activation may serve as a heat supply to change the thermal properties of the molten salts, which have efficient thermal conductivity. The ions in the Na salts accelerated the breaking of chemical bonds in the hydrochar precursors, thereby affecting the surface chemistry of the activated samples [51]. N 1s spectrum identified pyridinic N (N-6, (398.4 ± 0.1) eV), pyrrolic N (N-5, (400.2 ± 0.2) eV), graphitic N (N–Q, (401.5 ± 0.2) eV), and pyridine-N-oxide (N–O, (403.1 ± 0.3) eV) [49,52]. The relatively unstable N species, pyridine-N, and pyrrole-N, tend to form N–Q through depolymerization and rearrangement reactions as the pyrolysis temperature increases, considering the difference in thermal stability [53]. A higher N–Q content was obtained with the assistance of $NaHCO_3$, which indicated that the molten salt contributed to the reduction of the activation energy for cracking nitrogen-containing heterocycles and rebuilding the carbon matrix with a higher graphitization degree. The abrupt emergence of N–O in AHC-800 and AHP-800 indicated that free Na oxides, such as Na_2O, easily reacted with receptors located at the defect or edge of the carbon structure and grafted oxygen atoms onto N-6 to promote the removal of contaminants.

The detailed morphology and pore distribution of all samples were characterized by SEM, BET, and TEM analyses (Figs. S5 and S6 and Table S2 in Appendix A and Fig. 1(c)). A larger surface area, ranging from 133.11 to 844.62 $m^2 \cdot g^{-1}$, was obtained on activated hydrochars compared to precursors that possessed an almost nonporous nature (0.92–2.59 $m^2 \cdot g^{-1}$). The original HC and HP textures were reshaped through Na–salt corrosion into rough, porous, and hierarchical structures, which generated rich functional groups

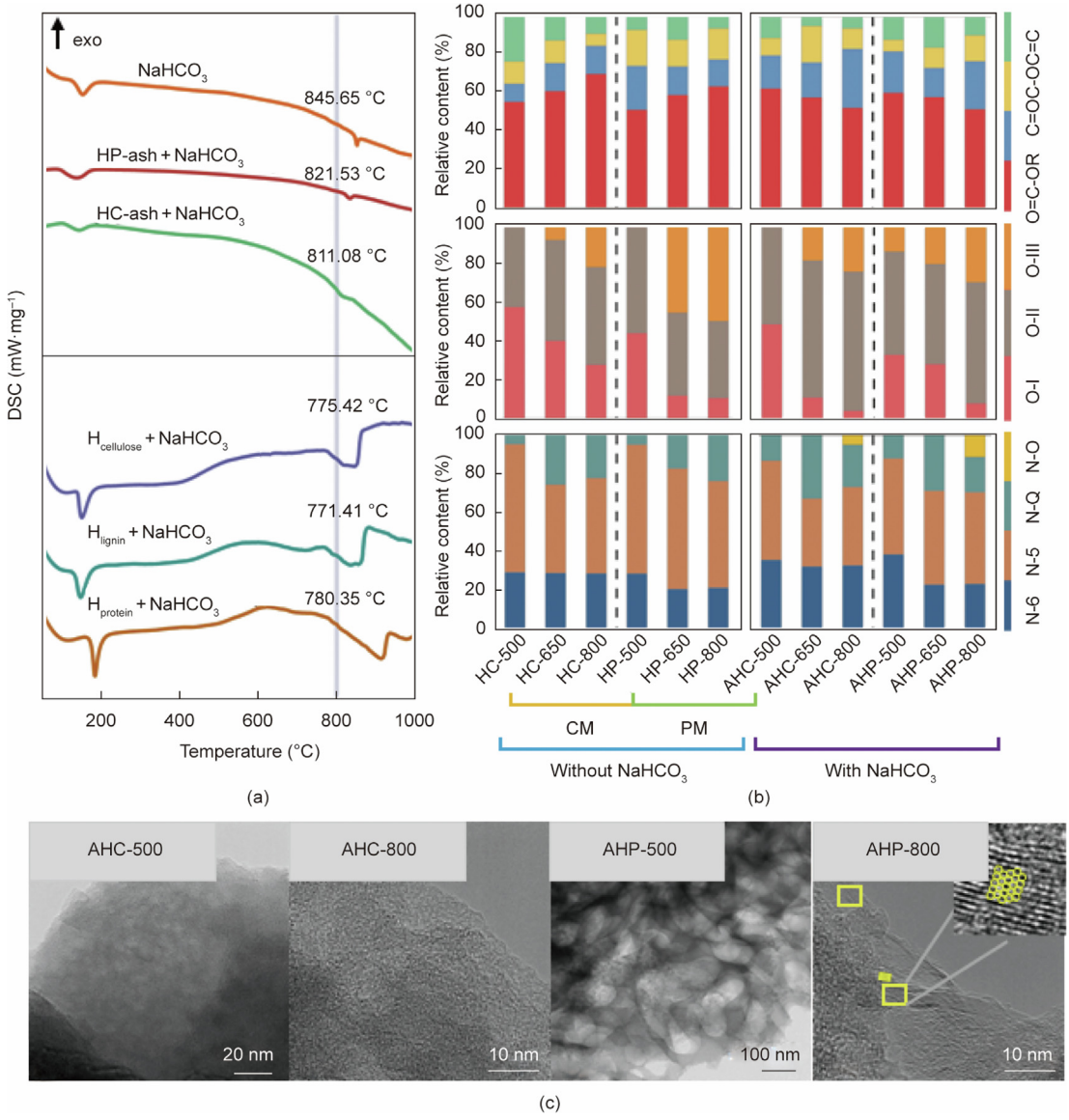

Fig. 1. (a) DSC analysis of $NaHCO_3$ and the mixture of $NaHCO_3$ with hydrochar compositions, wherein the grey line denoted the upper limit of activation temperature and the abbreviation exo stood for exothermic; (b) the proportion of each C, O, and N groups in hydrochar before and after activation; and (c) TEM images of activated hydrochar.

that acted as interfacial active sites. The cross-stacking of the striped graphite layers on AHP-800 indicates the presence of a uniform aromatic cluster. With excellent mobility to enclose feedstocks and catalytic performance, the liquid-state carbonate caused more expanded meso- and micro-pores and the formation of worm-like structures with intricate micro-tunnels on AHC-800 and AHP-800, offering additional adsorption sites and dispersive forces for NH_3 storage.

3.2. Ash transformation during the activation process

Distinct inorganic compounds mingled in the excrement during the manure harvesting process in livestock production (Fig. S7 in Appendix A). XRF analysis suggested that the hydrothermal treatment facilitated the transfer of soluble components in manure, such as Na- and K-containing salts, into the aqueous phase. Si salts (44.38%) dominated the inorganic phase of CM, whereas more P (34.33%) and Ca (40.01%) salts were observed in the PM hydrochar. Without adding activator, the ash contents of livestock manure increased after pyrolysis (43.09%–62.05%) (Fig. 2(a)), indicating the slim impact of acidic washing on ash removal. This can be attributed to the dehydrogenation and deoxidation of organic matter, resulting in a more compact carbon mantle after thermal treatment, significantly deterring total ash dissolution [54]. A carbon surface dominated by C, O, and N was observed through SEM-EDS (Fig. 2(b) and Table S3 in Appendix A), whereas the ash signals decreased as the pyrolysis temperature increased, which was inconsistent with the variation in the ash content described above. XRD analysis was performed to provide deeper scanning for the crystal morphology of the unactivated hydrochar (Fig. 2(c)). In addition to the characteristic peak of SiO_2, the appearance of diffraction peaks of acid-soluble substances, such as calcium iron oxide and K_2O, suggests that a large amount of ash was still embedded in the internal layer of the carbon structure, strongly demonstrating the protective model of carbon towards ash in manure hydrochar. Metal nanoparticles exhibit much better-ordered carbon structures with straight stacked graphitic layers via autocatalytic reactions with local organics [55].

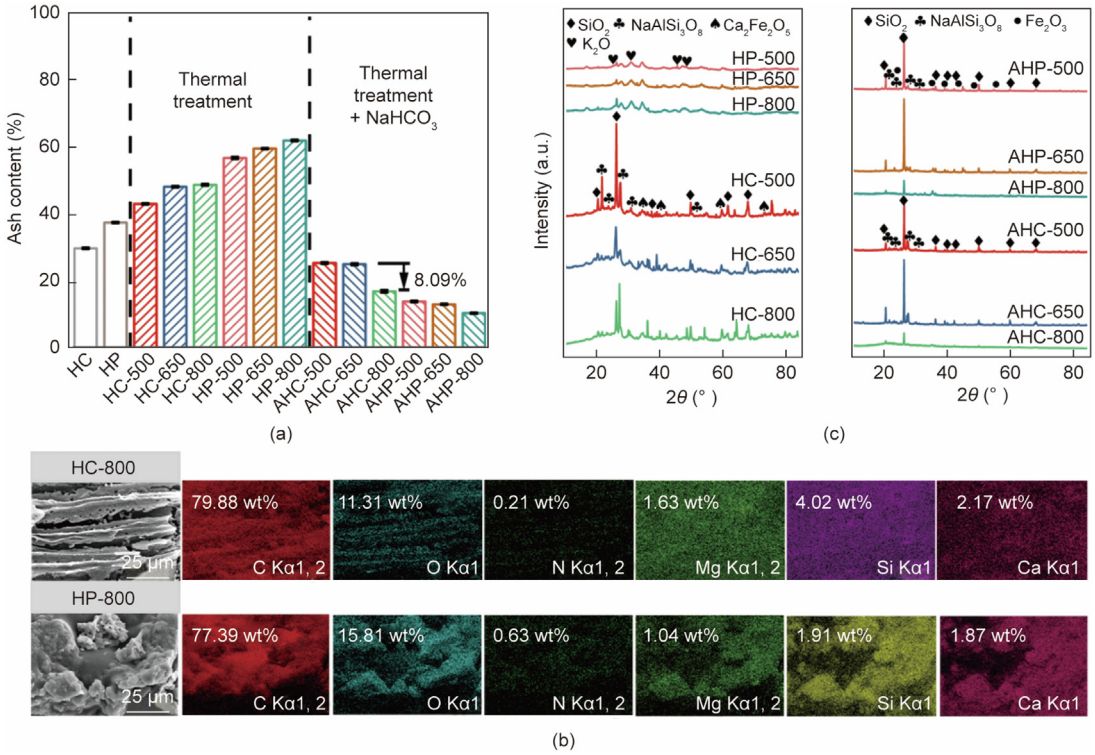

Fig. 2. (a) Ash content of carbon samples; (b) surface elements distribution of pyrolyzed hydrochars without $NaHCO_3$ via SEM-EDS analysis; and (c) XRD spectra of pyrolyzed hydrochars without activator and ash of activated hydrochar, wherein θ represented the angle of incidence of X-rays with respect to the crystal lattice plane and the abbreviation a.u. stood for arbitrary unit.

Lower ash contents (10.37%–25.40%) of activated samples indicated the effective destruction of carbon–ash complex structure by $NaHCO_3$ via catalyzing the successive aromatization of labile organic phase of hydrochar, thereby leading to the exposure of ash layers and considerable mineral loss after acid washing especially for metallic oxides. Notably, in contrast to the slight fluctuation for hydrochars activated at low temperatures, the significant decrease for AHC-800 and AHP-800 implies that the Na species contributed to the transformation of insoluble Si substances into soluble salts. The considerable dissolution of sodium silicate can be recycled to produce water glass and refractory materials [56]. From the XRD pattern (Fig. 2(c)), the ash composition of the activated hydrochars mainly contained SiO_2, Fe_2O_3, and $NaAlSi_3O_8$, among which the characteristic peaks of insoluble Na–salt compounds may have been caused by the high-temperature reactions between sodium oxide and Al/Si compounds. These reactions promote the dissolution of minerals and alter the presence of Si-containing species in the carbon structure as follows:

$$NaAlSi_3O_8 + 3Na_2O \rightarrow NaAlO_2 + 3Na_2SiO_3 \quad (1)$$

$$SiO_2 + Na_2O \rightarrow Na_2SiO_3 \quad (2)$$

$$P_2O_5 + 3Na_2O \rightarrow 2Na_3PO_4 \quad (3)$$

3.3. Breakthrough mechanism insight

The reactivity of metals in chemicals during activation affects the carbon structure and functionality. The $NaHCO_3$ was first decomposed at near 150 °C to generate CO_2 and Na_2CO_3, contributing to the physical damage of the original hydrochar structure and perforating with meso- and macro-pores [57]. The spiky curves at a pore size of 52 nm can be attributed to the loss of inorganic fractions (Fig. S6 in Appendix A). Limited by the absence of ion mobility, which was owing to the insufficiency of mechanical mixing and the agglomeration effect of ionic crystals, the activator etched carbon surface through solid–solid thermal contact and promoted gasification reaction for the development of mesopores in the range of 2–50 nm at relatively low catalytic temperatures (500 and 650 °C) (Figs. S5 and S6 in Appendix A). When the temperature reached 800 °C, the melting of sodium carbonate appeared early due to the interaction of functional groups with Na species. This liquid medium possesses high thermal conductivity and disperses the feedstock effectively, improving the regional heat transfer and activation performance in dynamic solid/liquid interfaces [58,59]. The carbon lattice expansion caused by the intercalation reaction of metallic Na and the release of various volatile substances (e.g., CO_2, CO, H_2O, and vaporized Na) during the process further enhanced the porosity of the hydrochar, particularly for the generation of micropores. A breakthrough mechanism for carbon–ash recalcitrance in manure hydrochar is proposed in Fig. 3.

The skeletal structure of manure hydrochar evolved from amorphous aromatic carbon clusters to a graphitic matrix with increasing pyrolysis temperature, sheltering the ash matter inlaid irregularly within the hydrochar by a compact carbon frame. The O-containing groups of hydrochar can interact with minerals via ligand exchange, cation bridges, hydrogen bonding, ion exchange, and van der Waals interactions, forming mineral-organic protective associations [60]. The introduction of $NaHCO_3$ resulted in the formation of a reaction region at a temperature range from 600 to 800 °C during the pyrolysis process (Fig. S2). In contrast to the relatively steady carbonization processes of the independent pyrolysis of HC and HP, the significant mass loss rates observed in the mixture of $NaHCO_3$ with HC and HP further demonstrated the enhanced cleavage of chemical bonds in the hydrochar

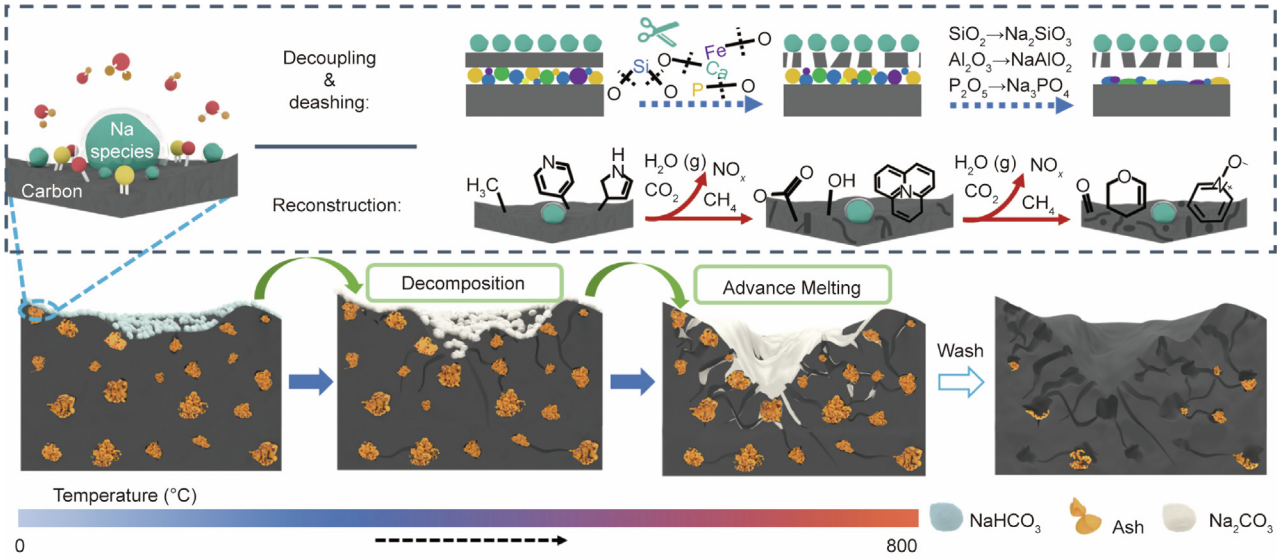

Fig. 3. Breakthrough mechanism of carbon–ash recalcitrance in manure hydrochar using $NaHCO_3$, wherein NO_x referred to nitrogen oxides.

precursors induced by activated molten salt ions. Engaging $NaHCO_3$ in activation accelerated carbon cracking and formed hierarchical channels to break the carbon–ash hybrid, exposing ash particles and depriving the protective effect of the organic phase on ash. The dissolution of ash is governed by the comprehensive interactions of inorganic components with carbon and Na salts, which significantly influence the structure and morphology of hydrochar and its environmental applications, such as adsorbents.

3.4. The NH_3 adsorption performance of the open structure

All samples activated could adsorb NH_3 effectively under dynamic adsorption conditions compared with the negligible adsorption capacities of inactivated hydrochars (0.71–6.83 $mg \cdot g^{-1}$) with almost vertical breakthrough curves (Figs. 4(a) and (b)). In addition, the mineral components exhibited slight contributions to NH_3 adsorption (Fig. S8 in Appendix A). This indicates that the sorption performance was dominated by the carbon surface chemistry and pore structure [61]. Despite the superior surface area and porosity, AHP-800 and AHC-800 showed the lowest adsorption capacities (10.83 and 11.82 $mg \cdot g^{-1}$ respectively) among activated hydrochars because of the shortage of heteroatoms which incurred the insufficient surface functionality and weak NH_3 affinity (Fig. 4(b)). Pores offer channels for NH_3 transmission, improving the utilization efficiency of surface-active sites, while the adsorption capability largely depends on the strength of adsorbent–adsorbate interaction [62–64]. Nevertheless, the hierarchical structures enhanced the pore diffusion of NH_3 and the armed hydrochar with rapid adsorption rates and surface reactivity. All samples displayed an evident decline trend for adsorption capacities as the temperatures elevated (Fig. 4(c)). This decline can be attributed to the increased adsorbate vapor pressure and adsorbed molecule energy level, which provided additional energy to enhance molecular vibration amplitude and induce a portion of the adsorbed NH_3 molecule surmounting the weak Van Der Waals force and escaping into the gas phase [65].

After pre-humidifying the carbon surface from 0 to 20%, there was an observed increase in the NH_3 adsorption capacities. Specifically, at room temperature, hydrochars activated at 500 and 650 °C exhibited enhanced capacities, ranging from 7.36% to 19.24% (Fig. 4(d)). The presence of H_2O facilitates proton transfer to NH_3 and the dissolution of NH_3. The formation of NH_4^+ in the water film strengthens NH_3 fixation on the pore walls by incorporating dissociated acidic functional groups through ion exchange [45]. Humidity negatively impacted the NH_3 uptake of AHC-800 and AHP-800, which could be ascribed to the condensed water vapor in the abundant micropores, limiting the direct interaction of NH_3 molecules with graphite layers via dispersive forces. NH_3 adsorption under humid conditions occurs via an NH_3 solubilization-like mechanism following Henry's law, which prevails when half of the micropore volume is filled with moisture [61]. The lack of surface polarity and blocking of micropores with water transcended the NH_3 dissolution effect and determined NH_3 capture significantly.

A multi-cycle adsorption test was performed to evaluate the engineering application potential of the hydrochars (Fig. 4(e)). The total NH_3 adsorption capacities of CM- and PM-activated hydrochars were 52.03–68.54 $mg \cdot g^{-1}$ and 51.17–100.49 $mg \cdot g^{-1}$ at 25 °C without prehumidification. Despite its maximum cumulative adsorption capacity after thermal regeneration, the adsorption capability of AHP-650 tumbled from 25.65 to 10.59 $mg \cdot g^{-1}$. Relatively low total adsorption attenuations were obtained on AHC-800 and AHP-800 at 36.53% and 42.83%, respectively (Fig. 4(f)). Notably, all the samples exhibited an obvious decline in the first-cycle adsorption; thereafter, the adsorbed amounts varied slightly. These results demonstrate that the cyclic NH_3 adsorption on hydrochars is limited by several steps. This inference was further verified by the poor relationship (R^2 = 0.77, P < 0.05) between (N + O)/C and total adsorption attenuation (Fig. 4(f) and Fig. S9 in Appendix A), indicating that the multi-cycle adsorption process was not dependent on the electronic environment at the interface between carbon and the adsorbate. The superior linear correlations of (N + O)/C and the volume ratio of mesopore to total pore (V_{meso}/V_{total}) with first-round adsorption attenuation (R^2 = 0.93, P < 0.05) and subsequent round adsorption attenuation (R^2 = 0.90, P < 0.05) revealed that ① the electron donor–acceptor interactions of heteroatoms with NH_3 molecule played an important role during adsorption which provided strong forces to stabilize the NH_3 bonding; ② the mesopores served as transmission channels for the diffusion process of erratic adsorbates, which interacted with carbon surface via weak interaction such as Van Der Waals force and H-bonding, from external surfaces to internal active sites, contributing to the mass transfer of NH_3 at the solid–gas interface during adsorption–desorption process. Compared to the literatures

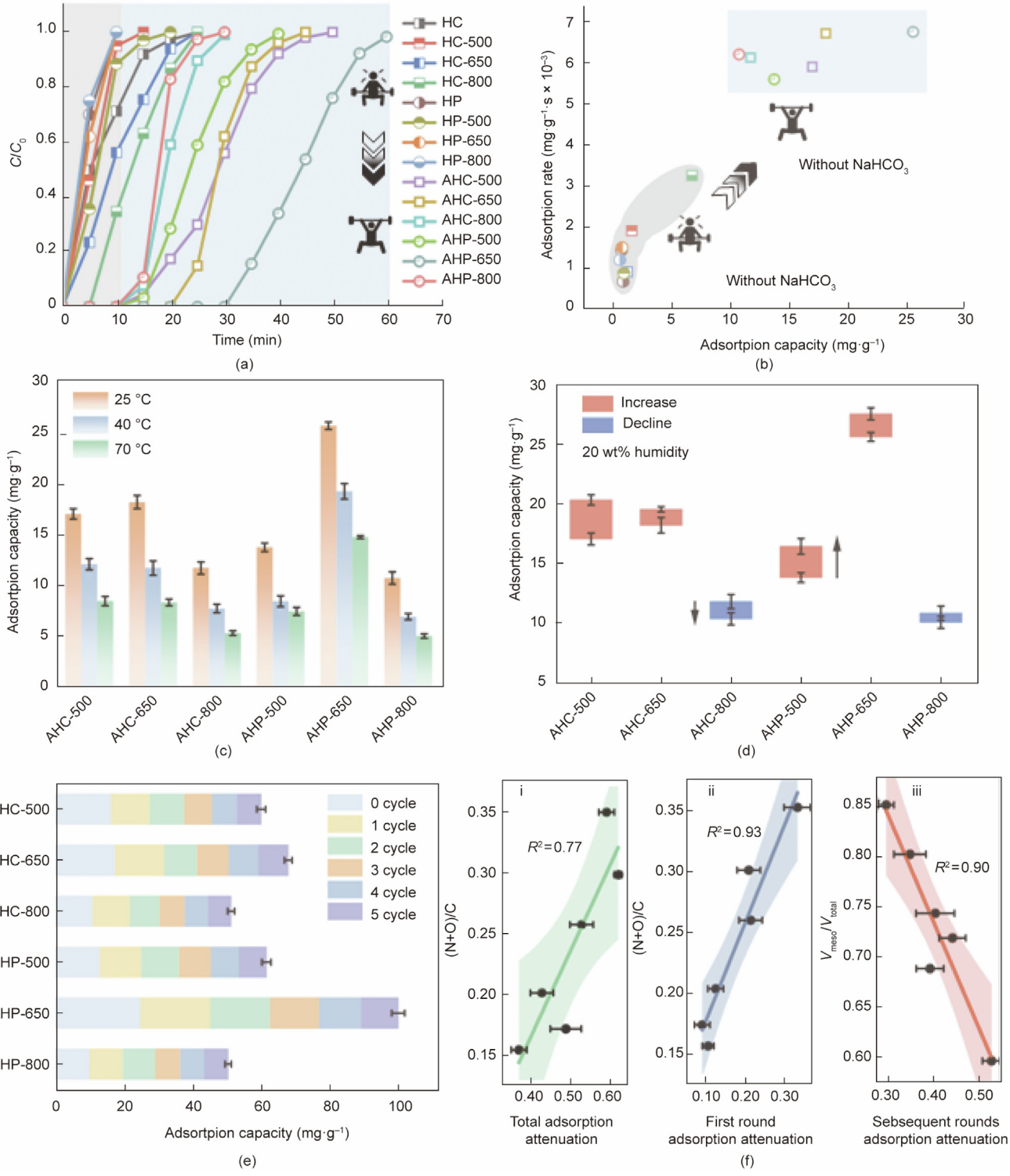

Fig. 4. Time-dependent (a) NH_3 adsorption breakthrough curves and (b) adsorption capabilities of hydrochars with and without $NaHCO_3$ treatment (at 25 °C, 0 wt%); (c) The temperature effect on NH_3 adsorption capacities of hydrochars; (d) NH_3 uptake on 20 wt% prehumidified carbon surfaces; (e) The NH_3 adsorption performance with recycled activated hydrochars during 5 cycles; and (f) the relationships of adsorption attenuations with surface polarity and pore distribution, where the subplots (i), (ii), and (iii) depicted the correlation of total adsorption attenuation with (N + O)/C, the dependence of first round adsorption attenuation on (N + O)/C, and the relationship between subsequent rounds adsorption attenuation and V_{meso}/V_{total}, respectively.

(Table 1 [45,63,71–77]), the activated manure hydrochar in this study had a favorable NH_3 adsorption capacity and significantly superior performance to commercial activated carbon. $NaHCO_3$-activated hydrochar from livestock waste is a promising green and low-cost adsorbent for NH_3 capture.

3.5. The role of exposed functional groups on NH_3 retention

To further explore the adsorption mechanism of NH_3 on the carbon surface, the N 1s and O 1s spectra of the adsorbed/desorbed samples were analyzed using XPS (Figs. S10 and S11 in Appendix

Table 1
NH_3 adsorption performance of different materials.

Raw materials	Adsorbents	Activators	Analysis condition	Measurement type	Adsorption capacity ($mg \cdot g^{-1}$)	Feature	References
Coconut	Commercial activated carbon	—	0.6–2.4 $mg \cdot g^{-1}$ NH_3, 0 relative humidity, 40–120 °C	Fixed bed	0.60–1.80	Negative correlation between adsorption capacity and adsorption temperature	[72]
Coal, wood, and coconut	Activated carbon	$ZnCl_2$, $CuCl_2$, vanadium and molybdenum oxides, hydroxyaluminium and hydroxyaluminium-zirconium polycations	1 $mg \cdot g^{-1}$ NH_3, 70% relative humidity, room temperature	Fixed bed	1.40–70.00	Importance of proper combinations of the strength, type, and number of functional groups	[71]
Coconut	Activated carbon	HNO_3, H_2SO_4, HCl, H_3PO_4 and CH_3COOH	10 $mg \cdot g^{-1}$ NH_3, 80% relative humidity, 30 °C	Fixed bed	2.27–41.65	Predomination of the total amount of acidic groups	[73]
Phenol-formaldehyde novolac	Activated carbon	HNO_3	1 $mg \cdot g^{-1}$ NH_3, 0 or 70% relative humidity, prehumidified 20–70 wt%, 23 °C	Fixed bed	1.90–20.10	Prevalence for the Brønsted and Lewis acid-base interactions	[63]
Coconut	Activated carbon	Ammonium metatungstate and ammonium molybdate	1 $mg \cdot g^{-1}$ NH_3, 70% relative humidity, room temperature	Fixed bed	0.90–5.70	Complexing effect and acid-base interactions of metallic sites	[74]
4-Ammonium styrene-sulfonic acid and 4-styrenesulfonic acid-*co*-maleic acid	Activated carbon	—	1 $mg \cdot g^{-1}$ NH_3, 0 relative humidity, room temperature	Fixed bed	3.20–44.00	The synergistic effect of N- and S-functional groups	[75]
Polymers	Activated carbon	H_2SO_4	1 $mg \cdot g^{-1}$ NH_3, 0 or 70% relative humidity, prehumidified 70 wt%, room temperature	Fixed bed	9.50–46.80	Oxidation of S-functional groups	[64]
CM	Hydrochar	H_3PO_4	0.35 $mg \cdot g^{-1}$ NH_3, 0 relative humidity, prehumidified 20 wt%, 25 °C	Fixed bed	6.02–19.89	Oxidation of P-functional groups	[45]
ZSM-5	Zeolites	Microporous organic polymers	4.5 $mg \cdot g^{-1}$ NH_3, 0–76% relative humidity, 20 °C	Fixed bed	1.60–6.40	Favorable cyclic adsorption performance on modified hydrophobic surface under humid conditions	[76]
Zirconium chloride and 1,4-benzenedicarboxylic acid	Metal-organic frameworks	2-Sulfo-1,4-benzenedi-carboxylic acid monosodium salt, 1,2,4,5-benzenetetra-carboxylic acid	2.876 $mg \cdot g^{-1}$ NH_3, 0 or 80% relative humidity, 20 °C	Fixed bed	24.65–48.11	Slow internal diffusion caused by overly bulky groups	[77]
CM and PM	Hydrochar	$NaHCO_3$	0.350 $mg \cdot g^{-1}$ NH_3, 0 relative humidity, prehumidified 0 or 20 wt%, 25–70 °C	Fixed bed	5.21–27.55, maximum 100.49 in five-cycle adsorption	Oxidation of N-functional groups, distinct contributions of open structure on multi-cycle adsorption	This study

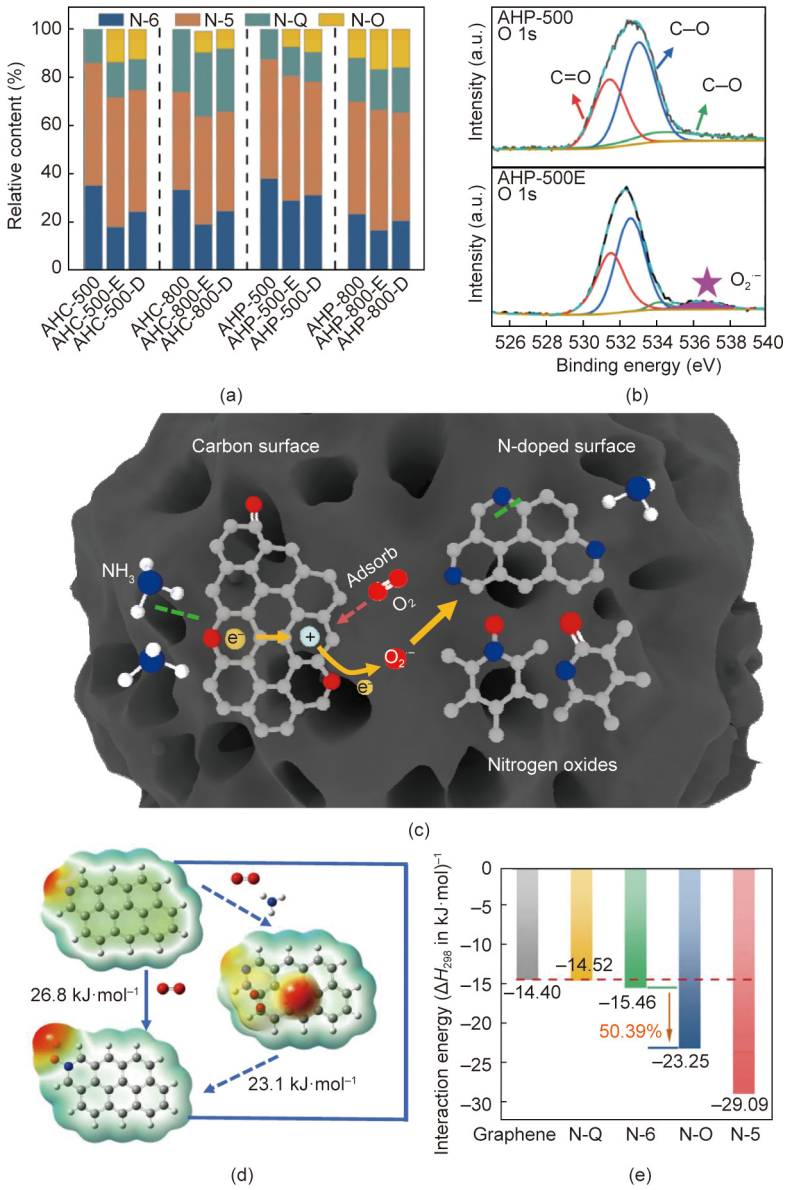

Fig. 5. (a) Distribution of N-containing groups of hydrochars before and after NH_3 adsorption and desorption, (b) XPS spectra of O1s for exhausted AHP-500, (c) the oxidation mechanism of N-doped carbon surface, (d) changes of excitation energy barrier of surface oxidation in the presence of NH_3, and (e) the interaction energy of NH_3 with N species.

A and Fig. 5(a)). The signal of chemisorbed oxygen species (O-IV), which suggested the generation of superoxide ions, materialized after exposure to NH_3 (Fig. 5(b)). Typically, the chemisorbed oxygen species are reduced to O_2^- in the presence of oxygen- and nitrogen-containing groups, such as hydroquinone, phenolic moiety, carbonyl, and pyridine-N groups, and oxidized the surface groups [66–68]. Electrons are captured and stored by the abundant functional moieties on the carbon surface and transferred to the adsorbate with a lower-lying unoccupied orbital for auto-redox reactions [69]. The lifespan of the free radicals mentioned above is short and vulnerable to environmental parameters. The higher relative content of O-IV was obtained on the hydrochar activated at 500 °C, which indicated that the presence of superoxide ions might be associated with the quantity and variety of functional groups. Accordingly, the hydrochar activated with $NaHCO_3$ derived from livestock waste led to an increase in the percentage of N–O (4.62%–11.25%) and a decrease in the percentage of N-6 (3.29%–12.18%) following NH_3 adsorption (Fig. 5(a)). The finding indicated the conversion of pyridine-N to pyridine-N-oxide after NH_3 adsorption, providing evidence that the oxidation of the heterogeneous nitrogen-doped carbon surface was triggered by O_2^-. This observation supports the assumption that incorporating NH_3 molecules on the carbon surface alters the electrostatic potential of the carbon structure, leading to electron accumulation on the adsorbed O_2 surface due to electron compensation by localized electrons (Fig. 5(c)). The graphite-like sheet with electron conductivity functioned as a bridge to shuttle electrons because the delocalized π electrons in aromatic rings could resonate and migrate mutually, facilitating the charge transfer [67,70].

The oxidation reaction occurring during NH_3 adsorption was further verified by DFT calculations (Fig. 5(d)). The introduction of the NH_3 molecule regulated the electron distribution in the delocalized π rings, which contributed to the transfer of electrons to oxygen because of the differences in valence electron and electronegativity of the O, N, and H atoms and reduced the Gibbs free energy of the oxidation process from 26.8 to 23.1 kJ·mol^{-1}. The distinct optimized conformations of carbon structures with NH_3 demonstrated that polar functional groups led to the stable affinity

of NH_3 through acid-base interaction and H-bonding [45,64,71], with the interaction energies varied from −14.40 to −47.29 kJ·mol^{-1} (Fig. S12 in Appendix A). The potential adsorption active sites in N-doped carbon structures derived from protein-rich animal manures differed owing to the distinct influences of the lone pair of electrons of the N atoms on the π electron conjugation system (Fig. S13 in Appendix A). NH_3 served as both the H-bonding acceptor and donor, wherein the interaction between the N atom in the NH_3 molecule and the H atom doped on the edge of the carbon surface exhibited a more robust adsorption force. The higher adsorption energy between pyridine-N-oxide and NH_3 revealed that the oxidation reaction intensified the NH_3 affinity because of the significant increase in charge accumulation and additional NH_3 binding sites (Fig. 5(e)). Incorporating additional oxygen atoms contributed to the shift of electrons from the carbon surface, enhancing the localized electron density, which triggered the strong chemisorption of NH_3.

4. Conclusion and further work

We used manure hydrochar activated with $NaHCO_3$ for NH_3 capture through a dynamic adsorption test. We found that the carbon–salt interaction altered the thermal characteristics of sodium carbonate, leading to more significant advanced melting than mixing with minerals. Molten sodium carbonate promoted the breaking of the carbon–ash protective relationship in high-ash hydrochar, significantly facilitating the dissolution of inorganic components and enhancing the quality of functional hydrochar from livestock manure. The swine manure hydrochar exhibited a maximum single adsorption capacity of 25.65 mg·g^{-1} and a five cycle overall adsorption capacity of 100.49 mg·g^{-1}. The presence of moisture facilitated the fixation of NH_3 on the hydrochar. Functional groups served as active sites, and surface oxidation simultaneously contributed to the excellent NH_3 uptake performance. Our results indicate that the oxidation of pyridine-N triggered by superoxide ions was mainly caused by electron transfer on the graphite layer after NH_3 incorporation, which is essential for understanding the response of the surface electronic environment of carbon materials to the NH_3 adsorption process. We clarified the relationship between multi-cycle adsorption performance, heteroatom doping, and pore structure, supporting the evaluation of the NH_3 adsorption capability of carbonaceous adsorbents in practical engineering application scenarios.

Understanding and improving the structure–application relationship of hydrochar plays an important role in designing functional hydrochar-based materials to address environmental issues. This work clarified how $NaHCO_3$ breaks the carbon–ash recalcitrance while ameliorating the surface chemistry and structure of hydrochar and investigated the adsorption and diffusion performance of NH_3 at the modified surface. Future research should focus on salt treatment. The wastewater produced after washing the hydrochar can be further valorized via cutting-edge technologies, such as electrocatalysis, porous medium evaporation, and ion exchange membranes, to recycle the molten salt ions and trace inorganic residues (e.g., silicon, calcium, phosphorus, and magnesium) derived from high-ash biomass, avoiding the potential environmental concerns of heavy metal accumulation and eutrophication. The separation, purification, and reuse of salt mixtures are necessary to minimize the cost of functional hydrochar fabrication. More rational model structures should be developed to better represent the chemical properties of hydrochar. Precise computational simulations require insightful studies of the main features of disorganized carbon structures to unveil the correlation between texture and performance.

Acknowledgements

This work was supported by the National Natural Science Foundation of China (52261145701, U21A20162) and the 2115 Talent Development Program of China Agricultural University.

Compliance with ethics guidelines

Zihan Wang, Leli Zhang, Yuanhui Zhang, and Zhidan Liu declare that they have no conflict of interest or financial conflicts to disclose.

Appendix A. Supplementary Data

Supplementary data to this article can be found online at https://doi.org/10.1016/j.eng.2024.01.009.

References

[1] Bleischwitz R, Spataru C, VanDeveer SD, Obersteiner M, van der Voet E, Johnson C, et al. Resource nexus perspectives towards the United Nations Sustainable Development Goals. Nat Sustain 2018;1(12):737–43.
[2] Vanhamäki S, Virtanen M, Luste S, Manskinen K. Transition towards a circular economy at a regional level: a case study on closing biological loops. Resour Conserv Recycling 2020;156:104716.
[3] Griggs D, Stafford-Smith M, Gaffney O, Rockström J, Öhman MC, Shyamsundar P, et al. Sustainable development goals for people and planet. Nature 2013;495(7441):305–7.
[4] Malyan SK, Kumar SS, Fagodiya RK, Ghosh P, Kumar A, Singh R, et al. Biochar for environmental sustainability in the energy–water–agroecosystem nexus. Renew Sustain Energy Rev 2021;149:111379.
[5] Xia L, Cao L, Yang Y, Ti C, Liu Y, Smith P, et al. Integrated biochar solutions can achieve carbon-neutral staple crop production. Nat Food 2023;4(3):236–46.
[6] Yu S, Dong X, Zhao P, Luo Z, Sun Z, Yang X, et al. Decoupled temperature and pressure hydrothermal synthesis of carbon sub-micron spheres from cellulose. Nat Commun 2022;13(1):3616.
[7] Zhang ZK, Zhu ZY, Shen BX, Liu LN. Insights into biochar and hydrochar production and applications: a review. Energy 2019;171:581–98.
[8] Huang JX, Feng YF, Xie HF, Wu P, Wang ML, Wang BY, et al. A bibliographic study reviewing the last decade of hydrochar in environmental application: history, status quo, and trending research paths. Biochar 2023;5(1):12.
[9] Tang CY, Yang F, Antonietti M. Carbon materials advancing microorganisms in driving soil organic carbon regulation. Research 2022;2022:9857374.
[10] Guo NN, Li M, Sun XK, Wang F, Yang R. Enzymatic hydrolysis lignin derived hierarchical porous carbon for supercapacitors in ionic liquids with high power and energy densities. Green Chem 2017;19(11):2595–602.
[11] Zhuo S, Ren H, Xie G, Xing D, Liu B. Conversion mechanism of biomass to nano zero-valent iron biochar: iron phase transfer and *in situ* reduction. Engineering 2023;21:124–34.
[12] Xiao X, Chen B, Chen Z, Zhu L, Schnoor JL. Insight into multiple and multilevel structures of biochars and their potential environmental applications. Crit Rev Environ Sci Technol 2018;52(9):5027–47.
[13] Jin J, Wang M, Cao Y, Wu S, Liang P, Li Y, et al. Cumulative effects of bamboo sawdust addition on pyrolysis of sewage sludge: biochar properties and environmental risk from metals. Bioresour Technol 2017;228:218–26.
[14] Li HG, Cao MJ, Watson J, Zhang YH, Liu ZD. *In situ* hydrochar regulates Cu fate and speciation: insights into transformation mechanism. J Hazard Mater 2021;410:124616.
[15] Yoshida S, Ohnishi Y, Kitagishi K. Histochemistry of silicon in rice plant. Soil Sci Plant Nutr 1962;8(1):36–41.
[16] Shen HS, Sundstøl F, Eng ER, Eik LO. Studies on untreated and urea-treated rice straw from three cultivation seasons: 3. Histological investigations by light and scanning electron microscopy. Anim Feed Sci Technol 1999;80(2):151–9.
[17] Cantrell KB, Hunt PG, Uchimiya M, Novak JM, Ro KS. Impact of pyrolysis temperature and manure source on physicochemical characteristics of biochar. Bioresour Technol 2012;107:419–28.
[18] Jin JW, Li YN, Zhang JY, Wu SC, Cao YC, Liang P, et al. Influence of pyrolysis temperature on properties and environmental safety of heavy metals in biochars derived from municipal sewage sludge. J Hazard Mater 2016;320:417–26.
[19] Liu ZY, Wang ZH, Chen HX, Cai T, Liu ZD. Hydrochar and pyrochar for sorption of pollutants in wastewater and exhaust gas: a critical review. Environ Pollut 2021;268:115910.
[20] Nicolae SA, Au H, Modugno P, Luo H, Szego AE, Qiao M, et al. Recent advances in hydrothermal carbonisation: from tailored carbon materials and biochemicals to applications and bioenergy. Green Chem 2020;22(15):4747–800.
[21] Liu Z, Zhao X, Xu L, Peng Q, He X. A novel hierarchically lightweight porous carbon derived from egg white for strong microwave absorption. Engineering 2022;18:161–72.

[22] Li X, Wang R, Shao C, Li D, Bai S, Hou N, et al. Biochar and hydrochar from agricultural residues for soil conditioning: life cycle assessment and microbially mediated C and N cycles. ACS Sustain Chem & Eng 2022;10 (11):3574–83.
[23] Guo J, Chen B. Insights on the molecular mechanism for the recalcitrance of biochars: interactive effects of carbon and silicon components. Environ Sci Technol 2014;48(16):9103–12.
[24] Xu YL, Chen BL. Investigation of thermodynamic parameters in the pyrolysis conversion of biomass and manure to biochars using thermogravimetric analysis. Bioresour Technol 2013;146:485–93.
[25] Han L, Ro KS, Wang Y, Sun K, Sun H, Libra JA, et al. Oxidation resistance of biochars as a function of feedstock and pyrolysis condition. Sci Total Environ 2018;616:335–44.
[26] Wang Y, Xiao X, Xu Y, Chen B. Environmental effects of silicon within biochar (sichar) and carbon–silicon coupling mechanisms. Crit Rev Environ Sci Technol 2019;53(23):13570–82.
[27] Xiao X, Chen B, Zhu L. Transformation, morphology, and dissolution of silicon and carbon in rice straw-derived biochars under different pyrolytic temperatures. Environ Sci Technol 2014;48(6):3411–9.
[28] Zhu X, Liu Y, Qian F, Zhou C, Zhang S, Chen J. Role of hydrochar properties on the porosity of hydrochar-based porous carbon for their sustainable application. ACS Sustain Chem Eng 2015;3(5):833–40.
[29] Gai C, Zhang F, Lang Q, Liu T, Peng N, Liu Z. Facile one-pot synthesis of iron nanoparticles immobilized into the porous hydrochar for catalytic decomposition of phenol. Appl Catal B 2017;204:566–76.
[30] Zhu X, Sun M, Zhu X, Guo W, Luo Z, Cai W, et al. Molten salt shielded pyrolysis of biomass waste: development of hierarchical biochar, salt recovery, CO_2 adsorption. Fuel 2023;334:126565.
[31] Xie YP, Yang HP, Zeng K, Zhu YJ, Hu JH, Mao QT, et al. Study on CO_2 gasification of biochar in molten salts: reactivity and structure evolution. Fuel 2019;254:115614.
[32] Shen JH, Hu HY, Xu M, Liu H, Xu K, Zhang XJ, et al. Interactions between molten salts and ash components during Zhundong coal gasification in eutectic carbonates. Fuel 2017;207:365–72.
[33] Chen W, Gong M, Li KX, Xia MW, Chen ZQ, Xiao HY, et al. Insight into KOH activation mechanism during biomass pyrolysis: chemical reactions between O-containing groups and KOH. Appl Energy 2020;278:115730.
[34] Sajjadi B, Zubatiuk T, Leszczynska D, Leszczynski J, Chen WY. Chemical activation of biochar for energy and environmental applications: a comprehensive review. Rev Chem Eng 2019;35(7):777–815.
[35] Egun IL, He HY, Hu D, Chen GZ. Molten salt carbonization and activation of biomass to functional biocarbon. Adv Sustainable Syst 2022;6(12):2200294.
[36] Frangini S, Masi A. Molten carbonates for advanced and sustainable energy applications: part I. Revisiting molten carbonate properties from a sustainable viewpoint. Int J Hydrogen Energy 2016;41(41):18739–46.
[37] Gomez-Vidal JC, Morton E. Castable cements to prevent corrosion of metals in molten salts. Sol Energy Mater Sol Cells 2016;153:44–51.
[38] Li B, Tang JZ, Xie X, Wei JT, Xu DL, Shi L, et al. Char structure evolution during molten salt pyrolysis of biomass: effect of temperature. Fuel 2023;331:125747.
[39] Frisch MJ, Trucks GW, Schlegel HB, Scuseria GE, Robb MA, Cheeseman JR, et al. Gaussian 16, revision A.03 [software]. Wallingford CT: Gaussian, incorporated; 2016.
[40] Lu T, Chen F. Multiwfn: a multifunctional wavefunction analyzer. J Comput Chem 2012;33(5):580–92.
[41] Raeva AA, Dongari N, Artemyeva AA, Kozliak EI, Pierce DT, Seames WS. Experimental simulation of trace element evolution from the excluded mineral fraction during coal combustion using GFAAS and TGA-DSC. Fuel 2014;124:28–40.
[42] Ding DH, Yang SJ, Qian XY, Chen LW, Cai TM. Nitrogen-doping positively whilst sulfur-doping negatively affect the catalytic activity of biochar for the degradation of organic contaminant. Appl Catal B 2020;263:118348.
[43] Ferrari AC, Robertson J. Interpretation of Raman spectra of disordered and amorphous carbon. Phys Rev B Condens Matter Mater Phys 2000;61 (20):14095–107.
[44] Yan XC, Jia Y, Yao XD. Defects on carbons for electrocatalytic oxygen reduction. Chem Soc Rev 2018;47(20):7628–58.
[45] Wang Z, Liu Z, Yuan C, Zhao X, Zhang Y, Liu Z. Construction of a novel closed-loop livestock waste valorization paradigm: bridging manure and ammonia gas via phosphate-doped hydrochar. ACS EST Eng 2022;2(9): 1732–44.
[46] Pan YK, Xu H, Chen MQ, Wu KD, Zhang YY, Long DH. Unveiling the nature of room–temperature O_2 activation and $O_2^{\bullet-}$ enrichment on MgO-loaded porous carbons with efficient H_2S oxidation. ACS Catal 2021;11(10):5974–83.
[47] Liu ZY, Wang ZH, Tang S, Liu ZD. Fabrication, characterization and sorption properties of activated biochar from livestock manure via three different approaches. Resour Conserv Recycl 2021;168:105254.
[48] Zhou ZY, Liu P, Wang S, Finfrock YZ, Ye ZH, Feng Y, et al. Iron-modified biochar-based bilayer permeable reactive barrier for Cr(VI) removal. J Hazard Mater 2022;439:129636.
[49] Yang JJ, Wang JL, Li H, Deng YR, Yang C, Zhao Q, et al. Nitrogen-doped biochar as peroxymonosulfate activator to degrade 2,4-dichlorophenol: preparation, properties and structure–activity relationship. J Hazard Mater 2022;424:127743.
[50] Wang YF, Zuo SL, Yang JX, Yoon SH. Evolution of phosphorus-containing groups on activated carbons during heat treatment. Langmuir 2017;33 (12):3112–22.
[51] Liu W, Jiang H, Yu H. Development of biochar-based functional materials: toward a sustainable platform carbon material. Chem Rev 2015;115 (22):12251–85.
[52] Lian F, Cui GN, Liu ZQ, Duo L, Zhang GL, Xing BS. One-step synthesis of a novel N-doped microporous biochar derived from crop straws with high dye adsorption capacity. J Environ Manage 2016;176:61–8.
[53] Zhao A, Liu SJ, Yao JG, Huang FP, He ZS, Liu J. Characteristics of bio-oil and biochar from cotton stalk pyrolysis: effects of torrefaction temperature and duration in an ammonia environment. Bioresour Technol 2022;343:126145.
[54] Liu L, Yang X, Ahmad S, Li X, Ri C, Tang J, et al. Silicon (Si) modification of biochars from different Si-bearing precursors improves cadmium remediation. Chem Eng J 2023;457:141194.
[55] Liu H, Lyczko N, Nzihou A, Eskicioglu C. Incorporating hydrothermal liquefaction into wastewater treatment—part II: characterization, environmental impacts, and potential applications of hydrochar. J Clean Prod 2023;383:135398.
[56] Kahlenberg V. Structural chemistry of anhydrous sodium silicates—a review. Chimia (Aarau) 2010;64(10):716–22.
[57] Deng J, Xiong TY, Xu F, Li MM, Han CL, Gong YT, et al. Inspired by bread leavening: one-pot synthesis of hierarchically porous carbon for supercapacitors. Green Chem 2015;17(7):4053–60.
[58] Koyasu K, Ohtaki T, Misaizu F. Temperature dependence of ion mobility of carbon cluster cations: intermediate region connecting low-and high-field conditions. Bull Chem Soc Jpn 2011;84(12):1342–6.
[59] Shang HS, Lu YJ, Zhao F, Chao C, Zhang B, Zhang HS. Preparing high surface area porous carbon from biomass by carbonization in a molten salt medium. RSC Adv 2015;5(92):75728–34.
[60] Yu S, Liu J, Yin Y, Shen M. Interactions between engineered nanoparticles and dissolved organic matter: a review on mechanisms and environmental effects. J Environ Sci (China) 2018;63:198–217.
[61] Kang DW, Ju SE, Kim DW, Kang M, Kim H, Hong CS. Emerging porous materials and their composites for NH_3 gas removal. Adv Sci 2020;7(24):2002142.
[62] Petit C, Bandosz TJ. Enhanced adsorption of ammonia on metal-organic framework/graphite oxide composites: analysis of surface interactions. Adv Funct Mater 2010;20(1):111–8.
[63] Zheng WH, Hu JT, Rappeport S, Zheng Z, Wang ZX, Han ZS, et al. Activated carbon fiber composites for gas phase ammonia adsorption. Microporous Mesoporous Mater 2016;234:146–54.
[64] Petit C, Kante K, Bandosz TJ. The role of sulfur-containing groups in ammonia retention on activated carbons. Carbon 2010;48(3):654–67.
[65] Le-Minh N, Sivret EC, Shammay A, Stuetz RM. Factors affecting the adsorption of gaseous environmental odors by activated carbon: a critical review. Crit Rev Environ Sci Technol 2018;48(4):341–75.
[66] Frackowiak E, Beguin F. Carbon materials for the electrochemical storage of energy in capacitors. Carbon 2001;39(6):937–50.
[67] Klüpfel L, Keiluweit M, Kleber M, Sander M. Redox properties of plant biomass-derived black carbon (biochar). Environ Sci Technol 2014;48(10):5601–11.
[68] Uchimiya M, Stone AT. Redox reactions between iron and quinones: thermodynamic constraints. Geochim Cosmochim Acta 2006;70(6):1388–401.
[69] Boehm HP. Free radicals and graphite. Carbon 2012;50(9):3154–7.
[70] Keiluweit M, Nico PS, Johnson MG, Kleber M. Dynamic molecular structure of plant biomass-derived black carbon (biochar). Environ Sci Technol 2010;44 (4):1247–53.
[71] Bandosz TJ, Petit C. On the reactive adsorption of ammonia on activated carbons modified by impregnation with inorganic compounds. J Colloid Interface Sci 2009;338(2):329–45.
[72] Rodrigues CC, de Moraes Jr D, Da Nobrega SW, Barboza MG. Ammonia adsorption in a fixed bed of activated carbon. Bioresour Technol 2007;98 (4):886–91.
[73] Huang CC, Li HS, Chen CH. Effect of surface acidic oxides of activated carbon on adsorption of ammonia. J Hazard Mater 2008;159(2–3):523–7.
[74] Petit C, Bandosz TJ. Removal of ammonia from air on molybdenum and tungsten oxide modified activated carbons. Environ Sci Technol 2008;42 (8):3033–9.
[75] Travlou NA, Seredych M, Rodríguez-Castellón E, Bandosz TJ. Insight into ammonia sensing on heterogeneous S- and N- co-doped nanoporous carbons. Carbon 2016;96:1014–21.
[76] Kang S, Chun J, Park N, Lee SM, Kim HJ, Son SU. Hydrophobic zeolites coated with microporous organic polymers: adsorption behavior of ammonia under humid conditions. Chem Commun (Camb) 2015;51(59):11814–7.
[77] Jasuja H, Peterson GW, Decoste JB, Browe MA, Walton KS. Evaluation of MOFs for air purification and air quality control applications: ammonia removal from air. Chem Eng Sci 2015;124:118–24.